Cross section and analyzing power A_y in the breakup reaction $^2\mathrm{H}(\vec{p},pp)n$ at 65 MeV: Collinearity configurations

M. Allet, K. Bodek,* W. Hajdas, J. Lang, R. Müller, O. Naviliat-Cuncic, J. Sromicki, and J. Zejma*
Institut für Teilchenphysik, Eidgenösiche Technische Hochschule, Zürich, Switzerland

L. Jarczyk, St. Kistryn, J. Smyrski, and A. Strzałkowski
Institute of Physics, Jagellonian University, Cracow, Poland

W. Glöckle, J. Golak,* and H. Witała*
Insitut für Theoretische Physik II, Ruhr-Universität, Bochum, Germany

B. Dechant and J. Krug
Insitut für Experimentalphysik I, Ruhr-Universität, Bochum, Germany

P. A. Schmelzbach
Paul-Scherrer-Institut, Villigen, Switzerland
(Received 9 December 1993)

Kinematically complete breakup cross section and proton analyzing power data for four different collinearity configurations (neutron at rest in the c.m. system) have been measured in the reaction $^2\mathrm{H}(\vec{p},pp)n$ at $E_p^{\mathrm{lab}} = 65$ MeV. The experimental data are compared with rigorous solutions of the Faddeev equations using the Argonne AV14, Bonn B, Nijmegen, and Paris potentials. While the overall agreement is quite good there exist distinct discrepancies between theoretical and experimental cross section and analyzing power data in some regions of phase space.

PACS number(s): 21.30.+y, 25.10.+s, 13.75.Cs, 24.70.+s

I. INTRODUCTION

One of the basic questions in nuclear physics deals with the nature of the two-nucleon ($2N$) interaction. While QCD cannot yet be solved in the nonperturbative regime, meson theory has achieved some maturity and provides realistic $2N$ forces, which are able to describe very well the great amount of $2N$ data. It is of interest to see whether these forces can also be used in systems where more than two nucleons interact. The simplest one, the three-nucleon system ($3N$), has always been considered as an ideal testing ground for our understanding of the $2N$ interactions. Assuming $2N$ forces only, the Hamiltonian for the $3N$ system is fixed. Does it describe the experimental $3N$ observables? Is it necessary to introduce additionally genuine $3N$ forces in the dynamics of the $3N$ system? Now, with the advent of supercomputers, the $3N$ Faddeev equations can be solved in a numerically rigorous way for any local or nonlocal $2N$ interaction [1,2]. Therefore, the meson-exchange dynamics in $2N$ forces can be tested reliably in the $3N$ system by comparing the results of such calculations with accurate experimental data.

In recent years many experiments have broadened the database for such studies. The elastic nucleon-deuteron (Nd) scattering measurements with proton and neutron beams play a dominant role here. A set of accurate proton-deuteron (pd) angular distribution data, below and above the breakup threshold, has been established [3–6]. In addition to the cross section, a strong experimental effort has been made to obtain a complete set of spin observables. The vector and tensor analyzing powers have been measured at various energies [3–7]. For the pd system, complicated polarization-transfer experiments have been performed, in which the polarization of the outgoing nucleon was measured [8,9]. Likewise the elastic neutron-deuteron (nd) scattering has been studied extensively and a remarkable experimental progress has been achieved through the accurate measurements of the neutron vector analyzing power [10–13]. A measurement of the neutron-to-neutron polarization-transfer coefficient is in progress [14]. Good data, however, for the nd cross section are still very scarce [15–17]. Our theoretical analysis based on precise solutions of the Faddeev equations using modern realistic $2N$ interactions showed that most of these elastic scattering data are very well described by theory. The only outstanding exception up to now is the low-energy nucleon-deuteron analyzing power, which poses a severe puzzle. It is still unclear whether the reason for the discrepancy lies in the ^3P_J $2N$ force components, which dominate that observable, or whether

*On leave from Institute of Physics, Jagellonian University, Cracow, Poland.

more complicated three-body dynamics is required [18].

Apart from the elastic scattering the nucleon-induced deuteron breakup, leading to three free outgoing particles, is another wide field for testing the $2N$ interactions. This process is even richer in physical information than elastic scattering. In these observables, the final momenta are not integrated over the deuteron wave function. The possibility of choosing specific kinematic configurations for the three outgoing nucleons allows one to concentrate on specific properties of the $2N$ interaction. Unfortunately, in the case of the breakup process the existing database is incomplete [19–27]. This statement is especially true for the neutron-induced breakup process and for *pd* breakup in the energy range above 25 MeV. Additionally, there exist discrepancies between results obtained by different groups [20–22,27]. The comparison with precise $3N$ Faddeev calculations revealed both very good agreement and also significant disagreement. A definite conclusion, whether additional dynamics beyond $2N$ forces are necessary, will only be possible once a well established database is available.

In this study we present a new set of cross section and analyzing power data for the proton-induced deuteron breakup reaction for various kinematically complete configurations at an incoming proton energy $E_p^{\rm lab} = 65.0$ MeV together with the predictions of rigorous Faddeev calculations based on different realistic $2N$ potentials. A particular effort was undertaken to get accurate values of the proton vector analyzing power. In view of the $3N$ calculations including $3N$ forces [28] that are expected to appear in the near future, such a set of accurate breakup data is very welcome. The existing data for this observable in the breakup process are scarce and, practically, limited to low energies. At about 10 MeV the nucleon analyzing power is small and the experimental data have large errors, which exclude a conclusive theoretical analysis [21,22].

In this paper we concentrate on four regions of phase space where one of the three outgoing nucleons (the neutron) is at rest in the c.m. system. These configurations, called "collinearity," are realized by measuring two protons in coincidence at appropriate laboratory angles. Such configurations are expected to be sensitive to three-nucleon force (3NF) effects. This was shown in a simple model study including a 3NF [29] at an energy around 10 MeV and more recently by calculations performed with realistic but still truncated $2N$ and $3N$ dynamics [28]. Furthermore, a Faddeev calculation in a collinearity configuration at 14.1 MeV [30] turned out to be quite insensitive to the choice of the $2N$ interaction and exhibited significant discrepancies with the experiment. It is therefore interesting to see if a similar behavior in collinearity configurations shows up at higher energies. Additionally, it is expected that the Faddeev calculations, which do not include the Coulomb force but are, nevertheless, applied to the *pd* system, are more reliable at higher energies.

In the next section we present the details of the experimental setup and data analysis. The theoretical calculations are briefly sketched in Sec. III. The results are discussed in Sec. IV. Conclusion and outlook are given in Sec. V.

II. EXPERIMENTAL PROCEDURE

A. Experimental setup

The experiment was carried out at the Philips Cyclotron in the Paul Scherrer Institute - Villigen, Switzerland. The cyclotron provided a transversally polarized proton beam with an energy of 65 MeV (±50 keV), an average intensity of about 300 nA, and a polarization $|P_y| = 0.75$. The beam was focused on a ^{12}C target mounted in a transmission polarimeter, and guided beyond to the reaction chamber and refocused on the deuterium gas target (beam spot diameter about 2 mm) and, finally, stopped in a Faraday cup. The polarimeter target was a 200-μg/cm^2-thick self-supporting carbon foil. Energy loss and angular straggling in the foil were small—2 keV and 0.1 mrad, respectively—so that the beam quality in the main reaction chamber was not affected. The beam polarization was continuously monitored by observing the asymmetry in $\vec{p}$+^{12}C elastic scattering at 45.8° (where $A_y = 0.9985$ [31]) with a pair of NaI(Tl) scintillation detectors. Every second the sign of the polarization was reversed by switching the radio-frequency transitions at the ion source.

A gas target and eight detectors were mounted in the horizontal plane of a scattering chamber (diameter 1200 mm) [32]. Its schematic view is shown in Fig. 1. The target, filled with deuterium gas (99.7% purity) to a pressure slightly higher than atmospheric, was cooled down by liquid nitrogen to 77 K in order to increase the gas density. The target container was a 224 × 30 × 50-mm^3 stainless-steel block, with a cylindrical channel of 16 mm diameter, installed with its long axis along the beam direction. Reaction products left the target through 12-μm-thick Kapton windows covering an angular range from 12° to 150° on both sides of the beam line. Thick target walls provided shielding of the detectors against particles scattered in the entrance and exit 3-μm-thick Havar windows. A gas monitoring system kept the target pressure on the

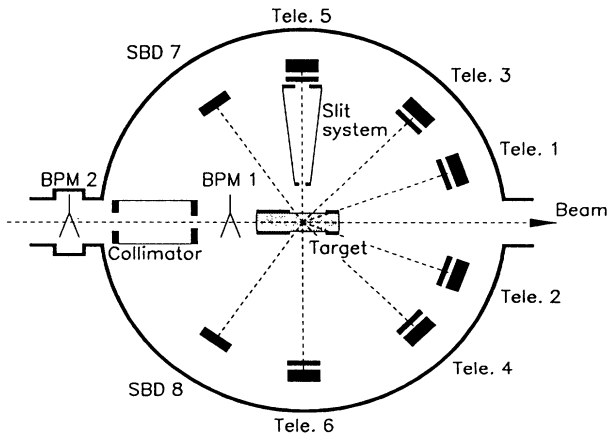

FIG. 1. Experimental setup in the scattering chamber—schematic diagram. The collimating system for only one detector is shown. BMP1 and BMP2 are the beam profile monitors.

preset level with an accuracy better than 5%. The effective target volume contributing to the recorded events was determined by the slit systems of the detectors. Two beam profile monitors were used to monitor the spatial location and focus of the beam.

To reduce systematic errors the detectors were arranged symmetrically on both sides of the beam axis. For the largest angles (116°) 3-mm-thick surface barrier (SB) detectors were used whereas the other detectors were ΔE-E telescopes built from NE102 plastic scintillators coupled to photomultiplier tubes (Philips XP2012). The thicknesses of the ΔE scintillators (2 and 1 mm) were optimized for the required energy range, whereas the thicknesses of the E scintillators (35 and 25 mm, respectively) were adjusted to stop elastically scattered protons. The FWHM of the elastic proton peak at 20° (61 MeV) was 1.1 MeV, including 0.4 MeV for the kinematical broadening due to the finite angular acceptance. Similarly, at 60° (38 MeV) the FWHM was 1.3 MeV with a kinematical broadening of 0.9 MeV.

The detector slit system, made of 7-mm-thick brass plates, was designed to guarantee an unambiguous determination of the solid angles and of the effective target thickness needed to determine the absolute value of the cross section. The breakup cross section was measured relative to the cross section for the p+^{2}H elastic scattering. To achieve this the slit apertures of only one detector of each coincidence pair defined uniquely the target volume for the detection of ejectiles while the second detector of the pair observed all coincident particles from this target volume (see Fig. 2). In this way, the effective target thickness and the solid angle of the first detector drop out in the ratio of breakup to elastic-scattering cross sections. The described procedure was applied for all detector pairs measuring collinearity configurations. The angular acceptances of the detectors were determined by the dimensions of the backward slits and varied between $\Delta\theta = 1.3°$ and $\Delta\phi = 7.0°$ for the most forward and $\Delta\theta = 1.8°$ and $\Delta\phi = 2.5°$ for the backward detectors. Each detector was shielded against particles coming from

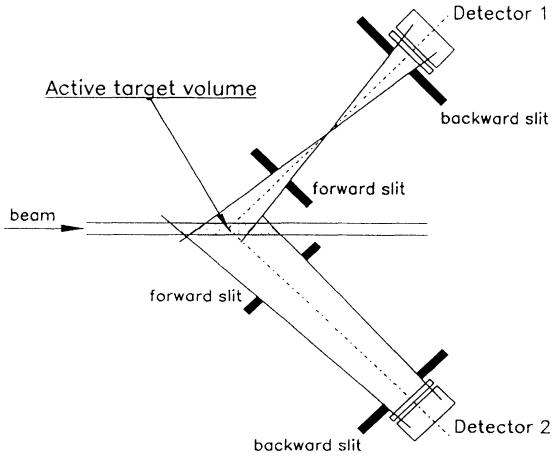

FIG. 2. Effective target volume. The collimator of detector 1 defines the target volume which is entirely seen by detector 2.

any direction other than that of the effective target volume.

Four collinearity configurations, $(\theta_1, \theta_2, \phi_{12}) = (20.0°, 116.2°, 180.0°)$, $(30.0°, 98.0°, 180.0°)$, $(45.0°, 75.6°, 180.0°)$, $(59.5°, 59.5°, 180.0°)$, were investigated. Other configurations, measured simultaneously, will be discussed in another paper.

The electronics and the data acquisition system allowed the measurement of all possible twofold coincidences between the detectors. Both energy and timing information were analyzed. The system recognized two kinds of events: coincidences between any two detectors (breakup events) and single detector events, recorded to normalize the breakup cross section, and scaled down to a rate acceptable for the data acquisition system (scaling factor of 1000). In both cases gate signals opened the ADC's for incoming analogue pulses and started the TDC's (stopped by the next cyclotron RF signal). The proton beam burst width (typically 3 ns) was monitored by measuring the time spectrum (with respect to the cyclotron RF signal) of protons elastically scattered from the polarimeter target with a plastic scintillation detector placed below the beam line. Fast electronics and charge-sensitive ADC's with short gates (50 ns) were used for processing the scintillator pulses with single count rates of up to 100 000 per s. The energy information from the SB detectors was handled by charge-sensitive preamplifiers and spectroscopy amplifiers coupled to voltage sensitive ADC's (the single count rate of the SB detectors was significantly lower). The TDC start signals from the SB detectors were derived with the help of timing filter amplifiers and constant fraction discriminators.

By adjusting the beam current the number of accidental coincidences was kept below 15% for the events along the three-body kinematical curve. In order to determine their amount accurately, purely random events were taken simultaneously with true coincidences. For this purpose a coincidence time window of 80 ns was used, which is long enough to accept the fastest protons induced by one beam burst and the slowest ones belonging to the subsequent one. Since the time of flights were also measured it was possible to distinguish the coincidences belonging to only one beam burst (true+random) from those where the detected particles belong to different beam bursts (purely random).

The data acquisition system consisted of a CAMAC based front end processor (ACC 2180) connected via ETHERNET to the μVAX back end computer. The events were recorded on magnetic tapes for off-line analysis. Each event contained a tagword characterizing the coincident pair of the detectors and the polarization sign, the pulse height of all signals from the selected detector pair, and the times with respect to the cyclotron RF signal. The event rate reached a value of up to 650 per s. The data were collected during about 400 h, divided into cycles of 2-h duration.

The energy calibration of the detectors was done using the elastic scattering of protons from protons and deuterons. For this purpose a series of single spectra were taken for angles increased successively in steps of 5°, with the target filled with a 1:1 mixture of hydro-

gen and deuterium gases. Background (empty and no target runs) and energy calibration measurements were performed every 20–30 h. The adjustment of the detector angles was checked by searching for the maximum of the ejectile proton-recoil deuteron coincidence rate as a function of the relative angle between the detectors.

B. Data analysis

In order to determine the kinetic energy of the measured protons a relation between this energy and the channel number registered in the E-detector ADC was established on the basis of calibration runs. The calibration was checked by a comparison of the two-dimensional kinetic energy E_1-E_2 coincidence spectra with the calculated three-body relativistic kinematics. Small corrections of the energy calibration (3% in the extreme case) were sometimes necessary mainly in the central regions of the kinematical curve. The main reason for these differences was gain changes during the calibration runs due to count rate variations as a function of the scattering angle. Gain variations during the regular runs (typically smaller than 1%) were eliminated before the analysis using the positions of the elastic peaks.

In order to eliminate as many as possible unwanted events, i.e., background and accidental coincidences, the following three conditions were imposed on the analyzed events during event selection: (a) particle identification (only protons were allowed, see Fig. 3), (b) true coincidence requirement ("true+random" window, see Fig. 4), and (c) kinematically allowed region (two-dimensional contour enclosing the kinematical band, see Fig. 5). After passing through these filters, the events were projected onto the central three-body kinematics divided into equal bins of 2-MeV width. The events were attributed to the closest bins. The selected events still

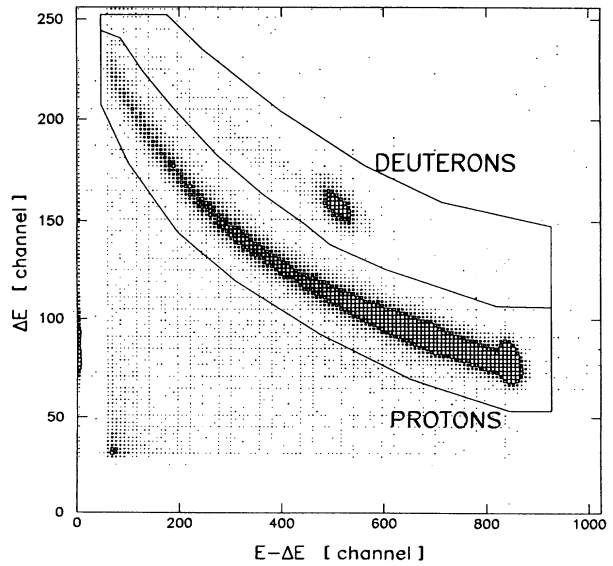

FIG. 3. Energy E-ΔE scatter plot with cuts defining the particle identification.

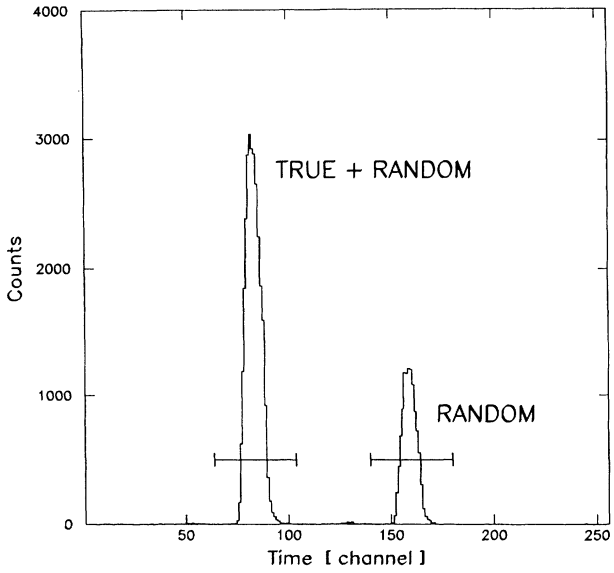

FIG. 4. Time-of-flight spectrum with windows for the identification of true+random and pure random events (1 channel =0.78 ns).

contained accidentals which had to be subtracted. The spectrum of accidentals was built in a procedure in which the coincidence time window enclosed a peak of pure accidentals (Fig. 4); the other filters were identical to those of "true+random" events. Outside the three-body kinematical band where no true events should occur the spectra

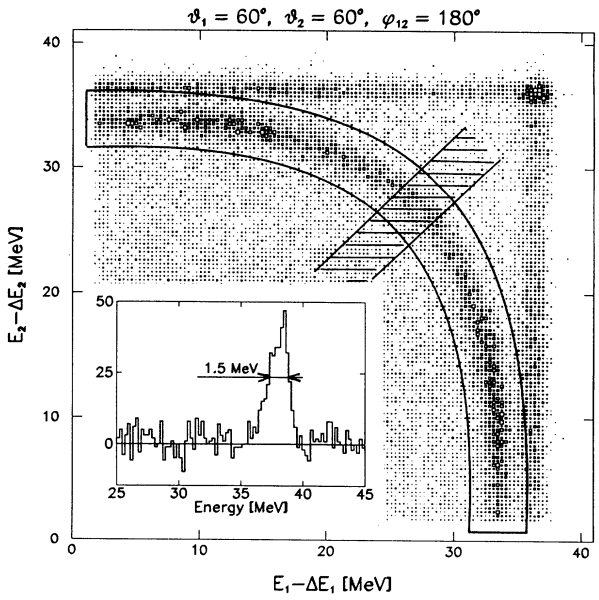

FIG. 5. E_1-E_2 spectrum of coincidences (true+random events) for the symmetric configuration (59.5°, 59.5°, 180.0°). The solid line represents a two-dimensional cut enclosing completely the kinematically allowed region (included finite geometry broadening and energy resolution of detectors). The inset contains a projection of the indicated slice cut perpendicularly to the kinematical band with subtracted random coincidences.

built with the "true+random" and "random" coincidence time windows were statistically identical.

For normalization purposes, the recoil deuterons from $p+^2$H elastic scattering were used. Events passing the particle identification filter were projected on the E axis of the stopping detector (Fig. 6). Results from test experiments proved that the low- and high-energy tails in the spectrum with almost constant but different intensities in the broad energy range were background, mainly caused by multiple scattering in which the target gas and the target walls were involved. Since the behavior of the background underlying the peak is unknown, it was assumed that it changes smoothly between the low- and high-energy sides of the peak. The errors in the background subtraction procedure were estimated to be less than 1.5%.

In the telescope set at 59.5° the deuteron peak was partially cut due to absorption in the ΔE scintillator and the elastically scattered protons had to be used for normalization in the symmetrical configuration (59.5°, 59.5°, 180.0°). The determination of the proton peak content in this case was less accurate (about 3%) since the proton spectrum also contains a continuum part from breakup events.

The polarization of the proton beam was determined using the rates in the $^{12}C(\vec{p},p)^{12}C$ elastic-scattering peaks for both polarization states in the left and right polarimeter detectors. In order to reduce the systemic errors caused by geometrical uncertainties, the mean asymmetry ϵ was calculated using the "superratio" technique, described below for breakup events. The value of the $^{12}C(\vec{p},p)^{12}C$ analyzing power [33] was rescaled using recent results from [31] resulting in $A_y = 0.9985 \pm 0.0015$. The beam polarization was very stable—its changes did not exceed 0.01—so an averaged value was used: $P_y = 0.758 \pm 0.004$. The error of the beam polarization was obtained by adding the squares of the statistical uncertainty of the mean asymmetry (0.002), the error of the analyzing power value, and systematic errors of the asymmetry measurement (0.003) [34,35].

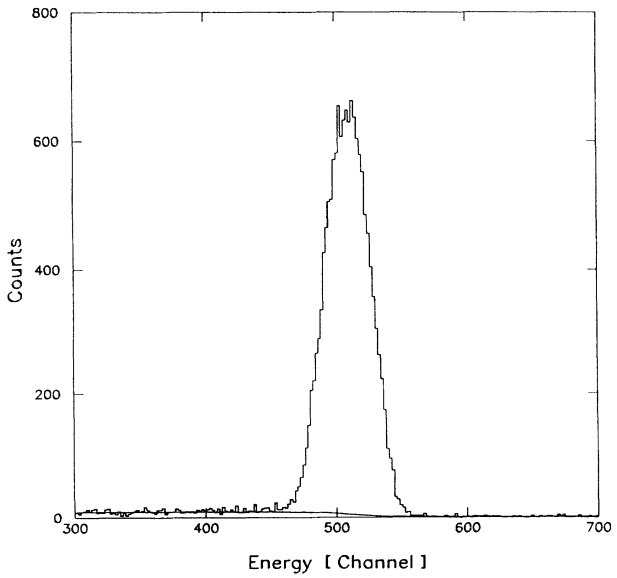

FIG. 6. Spectrum of recoil deuterons used for normalization of the breakup cross section. The solid line is a background fit outside the peak (see text).

In order to reduce geometrical errors which cannot be easily kept under control in coincidence experiments with a gas target, the breakup cross section was measured relative to the $p+^2$H elastic scattering. As mentioned earlier, the appropriately constructed slit system of the detectors guaranteed a unique definition of the effective target volume in the coincidence and normalization spectra, thus one solid angle drops out in the evaluation of the breakup cross section. The values of the elastic cross section were taken from a measurement by Shimizu *et al.* [6]. The breakup cross section was obtained from

$$\frac{d^3\sigma}{dS\,d\Omega_1 d\Omega_2}(S,\Omega_1,\Omega_2) = I(S,\Omega_1,\Omega_2)\frac{d\sigma_{\rm el}(\Omega_1)/d\Omega_1}{I_{\rm el}(\Omega_1)}(\Delta S\,\Delta\Omega_2)^{-1}\ , \quad (1)$$

where I is the breakup count rate in the interval ΔS at the point S along the three-body kinematical curve. The zero value of S was chosen at the crossing point between the kinematical curve and the E_1 axis. Similarly, $I_{\rm el}$ is the elastic-scattering count rate at the angle Ω_1. $\Omega_i = (\theta_i, \phi_i)$ are the polar and azimuthal coordinates of the ith detector, respectively, $\Delta\Omega_i$ being its solid angle and $d\sigma_{\rm el}(\Omega_1)/d\Omega_1$ is the elastic-scattering cross section. Since the breakup cross section was measured with a polarized proton beam, both I and $I_{\rm el}$ represent the breakup and the elastic-scattering count rate, respectively, summed over the proton spin-polarization states $(+,-)$ and averaged over the symmetrical detector pairs.

The analyzing power A_y along the three-body kinematical curve was calculated using the formula

$$A_y(S,\Omega_1,\Omega_2) = \frac{\epsilon}{P_y}\ , \quad (2)$$

where the asymmetry ϵ is defined as

$$\epsilon = \frac{r-1}{r+1}\ , \quad r^2 = \frac{I_L^+ I_R^-}{I_L^- I_R^+}\ .$$

I denotes the breakup count rate in the interval ΔS at the point S along the three-body kinematical curve for a given detector pair (L,R) and in a definite beam polarization state $(+,-)$, respectively. P_y is the value of the beam polarization. With this superratio technique the effects of almost all geometrical imperfections of the apparatus cancel to first order [36]. Experimental cross section and analyzing power data together with their uncertainties are presented in Figs. 7–10.

C. Experimental uncertainties

The experimental uncertainties are briefly discussed below. Table I summarizes only those which contribute

more than 0.25% to the cross-section values and 0.002 to the analyzing power. For statistical errors and uncertainties due to the angle setting the lower and upper limits are given.

The symmetrical configuration (59.5°, 59.5°, 180.0°) offers a test of the consistency of the experimental data. Parity-conservation forces the cross section to be symmetric and the analyzing power A_y to be antisymmetric with respect to the point $S = 44.3$ MeV on the kinematical curve. The asymmetry parameter $\epsilon_\sigma = (\langle\sigma\rangle_L - \langle\sigma\rangle_R)/(\langle\sigma\rangle_L + \langle\sigma\rangle_R)$ of the average experimental cross section on the left, $\langle\sigma\rangle_L$, and on the right, $\langle\sigma\rangle_R$, to that point is equal to 0.014 ± 0.013. Similarly, the absolute value of the average experimental analyzing power reveals the asymmetry,

$$\epsilon_A = (|\langle A_y\rangle_L| - |\langle A_y\rangle_R|)/(|\langle A_y\rangle_L| + |\langle A_y\rangle_R|) ,$$

of 0.18 ± 0.12. Both ϵ_σ and ϵ_A are fairly consistent with zero.

The averaged value of the solid angle of the second detector $\Delta\Omega_2$ depends on the target dimensions and enters explicitly into the cross-section formula. By numerical integration over the effective target volume it was found that the $\Delta\Omega_2$ values were within 0.05% equal to those

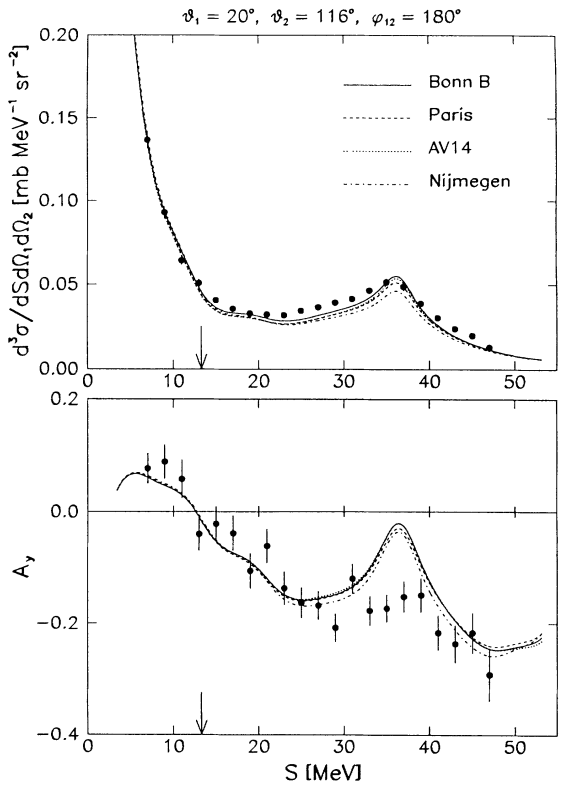

FIG. 7. Experimental cross section (a) and analyzing power A_y (b) for the collinearity configuration (20.0°, 116.2°, 180.0°). Error bars represent the total (statistical+systematical) experimental errors. Curves represent point geometry calculations obtained using four different $2N$ potentials: Bonn B (solid), Paris (dashed), Argonne AV14 (dotted), and Nijmegen (dash-dotted). The arrows show the positions of the collinearity points.

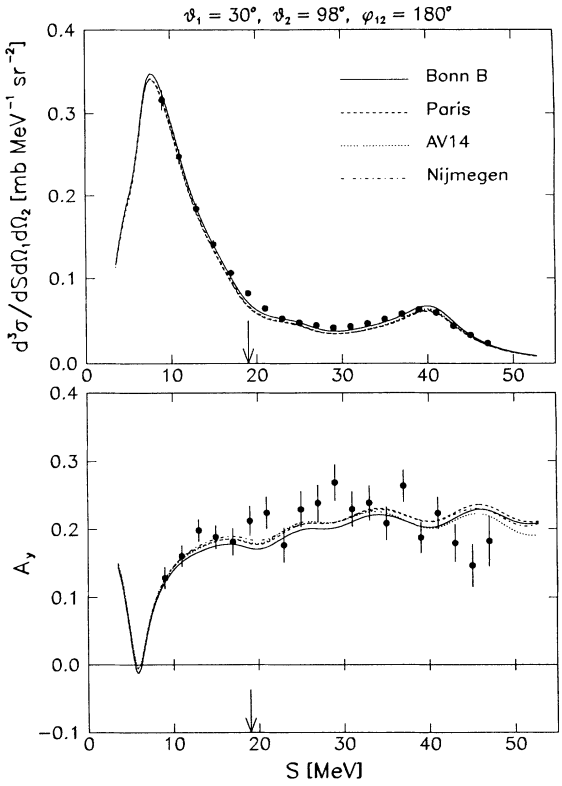

FIG. 8. Same as Fig. 7 but for the configuration (30.0°, 98.0°, 180.0°).

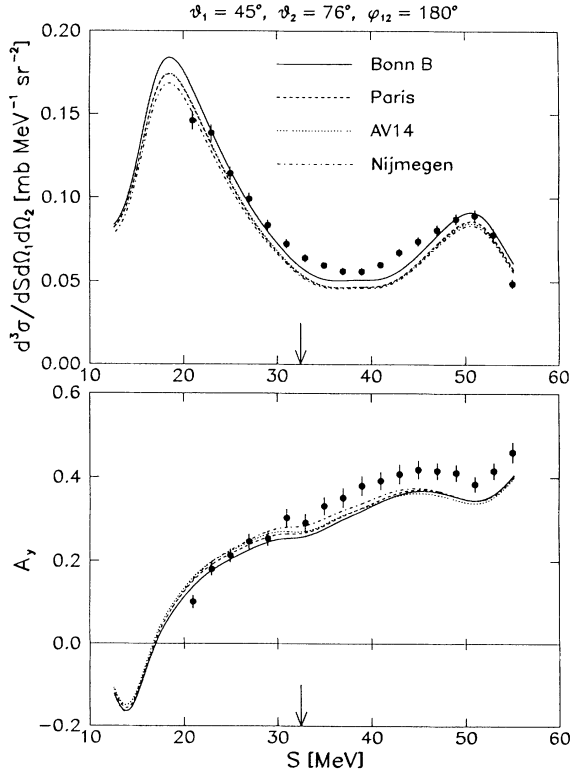

FIG. 9. Same as Fig. 7 but for the configuration (45.0°, 75.6°, 180.0°).

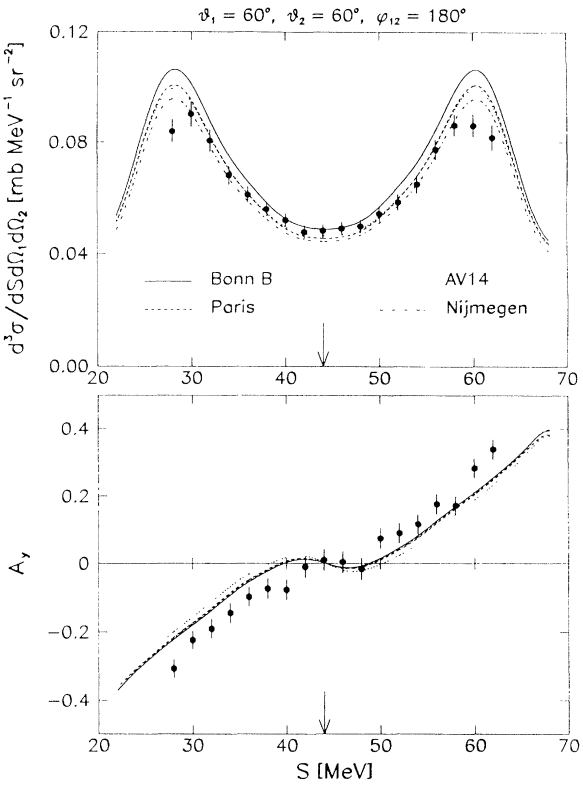

FIG. 10. Same as Fig. 7 but for the configuration (59.5°, 59.5°, 180.0°).

calculated from the center of the target. Their errors originate mainly from mechanical imperfections of the slits; they were estimated to be about 0.5%.

1. *Slit scattering and multiple scattering effects*

In order to estimate the influence of slit scattering and multiple scattering in the target on the breakup data, the two-dimensional contour which contained the three-body locus in the coincidence energy spectra (see Fig. 5) was varied. It was found that an increase of the window width by about 20% increases the number of true breakup counts by 1%. A similar result was obtained with the Monte Carlo program simulating the slit scattering effects for elastically scattered protons and deuterons. The number of slit scattering events under the elastic peak was found to be between 1 and 1.5 %. Thus, we conclude that slit and multiple-scattering effects influencing the breakup and elastic-scattering events partially compensate each other in the value of the breakup cross section. The entire error was conservatively assumed to be 1%. Slit scattering effects are negligible in the case of the analyzing power.

2. *Energy calibration uncertainties*

Uncertainties in the energy calibration can influence the position of the bin along the three-body kinematical curve and cause the deformation of the measured observable as a function of the arc length parameter S. Since the energy calibration had to be corrected for gain shifts during calibration runs, the upper limits for the errors due to the correcting procedure were found in the following way. For each configuration, the cross-section and analyzing power data were determined using both corrected and uncorrected calibrations. The differences between them were assumed to be equal to the uncertainties in the corrected energy calibration: on the average 1.5% for the cross section and 0.008 for the analyzing power.

3. *Dead time and pileup*

Dead-time losses in the electronics and in the acquisition system were of the order of a few percent. Event processing in the CAMAC system and in the front end computer yielded the biggest contribution to the dead-time losses. Therefore, after the detection of any event, the inputs of *all* ADC's were blocked until the event was read out. Thus the fraction of accepted events was the same for all kinds of processes involving different ADC

TABLE I. Summary of experimental uncertainties.

Source	Cross section uncertainties (%)	Analyzing power uncertainties
Statistical[a]	0.9–2.7	0.012–0.035
Angular uncertainty	0.0–5.1	0.0–0.011
Energy calibration[b]	1.5	0.008
Slit scattering	1.0	Negligible
Solid angle	0.5	No influence
Beam polarization	No influence	0.004
Elastic cross section	2.6(3.7)[c]	No influence
Total systematic	3.3–6.0 (4.2–6.5)[c]	0.009–0.014
Total statistical+systematic	3.4–6.6 (4.3–7.1)[c]	0.015–0.038

[a]Including subtraction of accidentals.
[b]Upper limit.
[c]For (59.5°, 59.5°, 180°).

combinations and the dead-time corrections drop out in the formulas used to calculate the cross section and analyzing power. The probability of pileups depends on the single detector count rate. In the E counters the chance for pileup reached about 1% at forward and 0.5% at backward angles. It was found that the influence of pileup events on the results was well below 0.2%.

4. Uncertainty in the angle determination

For the breakup reaction the uncertainties of setting the detector angles ($\pm 0.1°$) transform into systematic errors in the cross-section and analyzing power. In order to estimate the upper limit of them, the theoretical observables, described in detail in the next section, were calculated with angles of two coincident detectors shifted by $+0.1°$ and $-0.1°$, respectively (maximum of effect). In the collinearity point these shifts caused negligible effects. Larger effects, up to 5% in the cross section and 0.01 in the analyzing power, were found only in the vicinity of structures due to final-state interactions. The errors caused by angular uncertainties are included into the systematic errors, separately for each point along the three-body kinematics. From the angular distribution of the elastic p+^{2}H scattering data [6] it was found that the angular uncertainties cause a contribution to the normalization error in the cross section of 0.3%.

III. THEORETICAL CALCULATIONS

The experimental cross-section and analyzing power data have been compared with the predictions of rigorous $3N$ calculations using different realistic $2N$ interactions of various types: purely phenomenological and meson-exchange ones. The calculation has been performed by summing up the multiple-scattering series for three interacting nucleons which leads to the Faddeev-like equations:

$$T = tP + tPG_0T \ . \tag{3}$$

Here G_0 is the free $3N$ propagator and P denotes the sum of cyclical and anticyclical permutations of the three nucleons. The two-nucleon off-shell t matrix is generated by the chosen $2N$ interaction through the Lippmann-Schwinger equation. Once Eq. (3) has been solved the transition operator U_0 for the breakup process is simply obtained as

$$U_0 = (1 + P)T \ . \tag{4}$$

This operator relation is understood to be sandwiched between the incoming state, which is composed of the deuteron wave function and the momentum eigenstate for the nucleon-deuteron relative motion, and the outgoing state for three free nucleons. For details of our notation, the numerical method and the performance we refer to [2,37]. As $2N$ interactions we used the Argonne AV14 [38], Bonn B [39], Nijmegen [40], and Paris [41] potentials. The nucleons were allowed to interact in all partial-wave states carrying total $2N$ angular momenta $j \leq 3$ and total $3N$ angular momenta $J \leq \frac{25}{2}$. It will be shown that such a truncation is justified at the considered energy. Any effects of the pp Coulomb force in the $3N$ calculations were totally neglected.

The breakup observables in some specific regions of the phase space, particularly in the final-state interaction configurations, are very sensitive to the value of the scattering length in the state $^1S_0$. Since there are both np and pp pairs, which interact differently in this state, we treated this well established charge-independence breaking (CIB) effect in all calculations by including an admixture of the total $3N$ isospin $T = \frac{3}{2}$ component [42]. The different interactions for the np and pp systems in the state $^1S_0$ were chosen as follows. In case of the Argonne AV14 and Bonn B potentials, which in the state $^1S_0$ are fitted to the np scattering length ($a_{np}^{\mathrm{AV14}} = -23.67$ fm and $a_{np}^{\mathrm{Bonn\ B}} = -23.75$ fm), we used for the $^1S_0$ pp interaction a changed version of the Bonn B potential, which has been fitted to the pp scattering length [39] ($a_{pp}^{\mathrm{Bonn\ B}} = -17.66$ fm). For the Nijmegen and Paris potentials, which are fitted to the pp scattering length ($a_{pp}^{\mathrm{Nijmegen}} = -17.82$ fm and $a_{pp}^{\mathrm{Paris}} = -17.64$ fm), the $^1S_0$ np interaction was taken from the Bonn B potential.

Before comparing the measured observables with the theoretical results a Monte Carlo program, which simulated the conditions of the experiment and the procedures used for data evaluation, was run to study the influence of the instrumental averaging on the observables calculated with the Bonn B potential. The beam intensity profile, finite sizes of the target and detectors and their energy resolutions were included in the simulation. The energy spread of the beam was neglected. The generated breakup events were projected onto the three-body central kinematical curve according to the same procedure as used for the experimental data. For both, cross sections and analyzing powers, the averaging effects were found to be small; in general below 1% for the cross sections and smaller than 0.002 for the analyzing powers. The smallness of the averaging effects, especially if compared to the differences between theoretical calculations performed with different $2N$ potentials, justifies the use of the theoretical predictions for point geometry in the comparison with the experimental data.

A problem of more serious nature are relativistic effects. They are clearly visible already on a kinematical level by comparing the allowed loci of the kinetic energies of the two final nucleons evaluated nonrelativistically and relativistically. In Fig. 11, we show a typical example. The loci are separated by about 0.3 MeV and the corresponding total arc lengths differ by almost 3 MeV. While our strictly nonrelativistic theory delivers, of course, the observables along the nonrelativistic locus, measured by a nonrelativistic arc length, the experimental data appear necessarily along the relativistic locus. Thus, the question arises, how to compare theory and experiment. A convincing answer requires obviously a relativistic dynamical framework, which is presently not available. In this study we applied an approximate procedure as follows. For a certain point S on the relativistic locus we

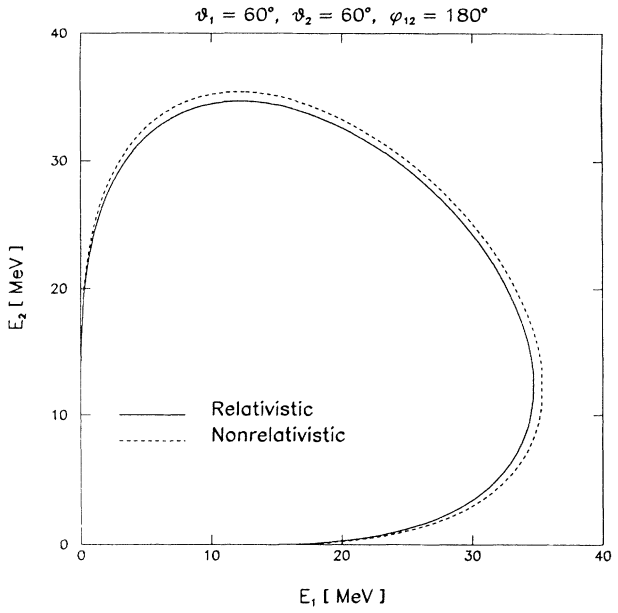

FIG. 11. Comparison of the relativistic (solid) and nonrelativistic (dashed) three-body kinematics for the configuration (59.5°, 59.5°, 180.0°).

choose the nearest point $S_{\rm nr}$ on the corresponding nonrelativistic locus and evaluate the value of the observable at that point. This simple method projects almost exactly (within 50 keV) the characteristic kinematical points [final-state interaction (FSI), quasifree scattering (QFS), collinearity] onto each other. The reliability of the projection method is also supported by the fact that the kinematical spread of the experimental data is larger than the average distance between the relativistic and nonrelativistic loci (see Fig. 5). A remark concerning the relativistic treatment of the phase-space factor is given in the next section.

IV. RESULTS OF CALCULATIONS AND COMPARISON WITH EXPERIMENTAL DATA

The theoretical predictions employing four different $2N$ potentials, i.e., Bonn B, Argonne AV14, Paris, and Nijmegen, are compared in Figs. 7–10 with our experimental results for the cross sections and the analyzing powers. The gross structure of the cross sections and their absolute magnitudes are well described by the theory. A similar statement holds for the analyzing powers. Also here the agreement in the general behavior is good. Going more into details, the following observations can be made.

(i) The calculated cross sections are sensitive to the potential used. Although similar in shape they differ in values from each other by up to 10% in some regions of phase space. While the results obtained with the Argonne AV14 and the Paris potential are very similar, the calculations with the Bonn B potential tend to be higher by up to 5%. Values lower by up to 4% are predicted for some S values by the Nijmegen potential. In contrast to the expectations based on low-energy results [30], the deviations are not smaller in the angular configurations where the conditions of collinearity are fulfilled.

(ii) The comparison between experiment and theory gives a rather variable picture. The best agreement over the whole arc length of the kinematical curve is achieved for the configuration $(30.0°, 98.0°, 180.0°)$. We notice that distinct structures predicted by the theory are less pronounced in the experimental data. For the smaller and larger θ_1 values (20° and 45°) the experimental cross section between the point of collinearity and the bump caused by the slope of a nearby FSI peak at the upper end of the arc length is higher by as much as 20%. The structure present in the theoretical analyzing power for the configuration $(20.0°, 116.2°, 180°)$ at around $S = 36$ MeV is absent in the experimental results. Unfortunately, it cannot be definitely ruled out by the experimental data with their present accuracy. For $\theta_1 = 45°$ and 59.5° the theoretical and experimental A_y's deviate clearly from each other.

(iii) If we restrict ourselves to regions near the exact collinearity configurations the deviations between theory and experiment are always small and do not surpass the differences which exist between the predictions by the different potentials. There is therefore not much room for contributions coming from genuine three-body forces and it will be interesting to see the outcome of future calculations including a 3NF.

The results shown in Figs. 7–10 are based on $2N$ forces with $2N$ subsystem angular momentum $j_{\rm max} = 3$ and $J_{\rm max} = \frac{25}{2}$ ($3N$ total angular momentum). In order to check the validity of this restriction we performed additional test calculations using the Bonn B potential. The inclusion of the $2N$ partial waves with $j = 4$ produces average changes in the cross section of 2% and the influence on the analyzing power is smaller than 0.01 (see Fig. 12). No difference between calculations with $J_{\rm max} = \frac{23}{2}$ and $J_{\rm max} = \frac{25}{2}$ could be recognized for the cross sections and the deviation in the analyzing power was again very small, ± 0.01.

As already stated, our theoretical calculations are strictly nonrelativistic both in the kinematical and dynamical parts. Although the relativistic kinematics in the phase-space factor ρ can be included, we believe that such a manipulation is not justified. Therefore, we present our theoretical results in a nonrelativistic form sticking to the nonrelativistic $\rho_{\rm nr}$. The values of the observables evaluated at a certain $S_{\rm nr}$ are identified with the values of the observables at the nearest S on the relativistic locus. If, however, one would like to see the relativistic corrections coming from ρ alone, one would have to multiply the presented theoretical cross sections by the ratios given in Fig. 13. They are calculated as follows: The phase-space factor is defined relativistically as

$$\rho(S) \equiv p_1 E_1 \int p_2^2 dp_2 \int d\mathbf{p}_3\, \delta(E - E_1 - E_2 - E_3)$$

$$\times \delta(\mathbf{P} - \mathbf{p}_1 - \mathbf{p}_2 - \mathbf{p}_3) \frac{1}{v} \frac{dE_1}{dS} , \qquad (5)$$

where $\mathbf{p}_i$ and $E_i = \sqrt{m_N^2 + \mathbf{p}_i^2}$ are the laboratory momenta and total energies of the three final nucleons, $\mathbf{P} = \mathbf{p}_N^{\rm lab}$ and $E = E_N^{\rm lab} + M_d$ are the total momentum and energy in the laboratory system expressed in terms of the momentum and energy of the initial nucleon and the deuteron mass M_d. $v = |\mathbf{p}_N^{\rm lab}|/E_N^{\rm lab}$ is the velocity of the initial nucleon and

$$\frac{dE_1}{dS} = \frac{1}{\sqrt{1 + (dE_2/dE_1)^2}} .$$

The nucleon momentum p_2 is evaluated as the zero of the energy-conserving δ function in (5) using either a relativistic or nonrelativistic form of energies. One arrives easily at [36]

$$\rho(S) = \frac{E_2 E_3 p_2^2 p_1 E_1}{|p_2 E_3 + E_2[p_2 - (\mathbf{P} - \mathbf{p}_1)\cdot\hat{\mathbf{p}}_2]|}\frac{E_N^{\rm lab}}{|\mathbf{P}|} \times \frac{1}{\sqrt{1 + \{[E_3 - (\mathbf{P} - \mathbf{p}_1 - \mathbf{p}_2)\cdot\hat{\mathbf{p}}_1(E_1/p_1)]/[E_3 - (\mathbf{P} - \mathbf{p}_1 - \mathbf{p}_2)\cdot\hat{\mathbf{p}}_2(E_2/p_2)]\}^2}} . \quad (6)$$

The nonrelativistic approximation thereof is

$$\rho_{\rm nr}(S_{\rm nr}) = \frac{m_N^2 p_2^2 p_1}{2p_2 - (\mathbf{P} - \mathbf{p}_1)\cdot\hat{\mathbf{p}}_2}\frac{m_N}{|\mathbf{P}|}\frac{1}{\sqrt{1 + \{[2p_1p_2 - (\mathbf{P} - \mathbf{p}_2)\cdot\hat{\mathbf{p}}_1 p_2]/[2p_1p_2 - (\mathbf{P} - \mathbf{p}_1)\cdot\hat{\mathbf{p}}_2 p_1]\}^2}} . \quad (7)$$

We cannot compare (6) and (7) directly since the arc lengths S and $S_{\rm nr}$ are different. $S_{\rm nr}$ is again projected onto the nearest point on S. In Fig. 13 the ratios $\rho(S)/\rho_{\rm nr}(S_{\rm nr})$ are shown for four collinearity configurations. The deviations from 1.0 are significant and extend to 10%. This is alarming but we should not draw the conclusion that these are the relativistic corrections for the cross sections at our energy of 65 MeV. The nuclear matrix element itself also depends on energy and changing its value according to the relativistic kinematics will certainly lead to a modification, whose magnitude is presently totally unknown. It might go in the same or opposite direction with respect to changes of ρ. The theoretical analyzing powers as ratios are of course independent of ρ and not influenced by such simple relativistic kinematical modifications.

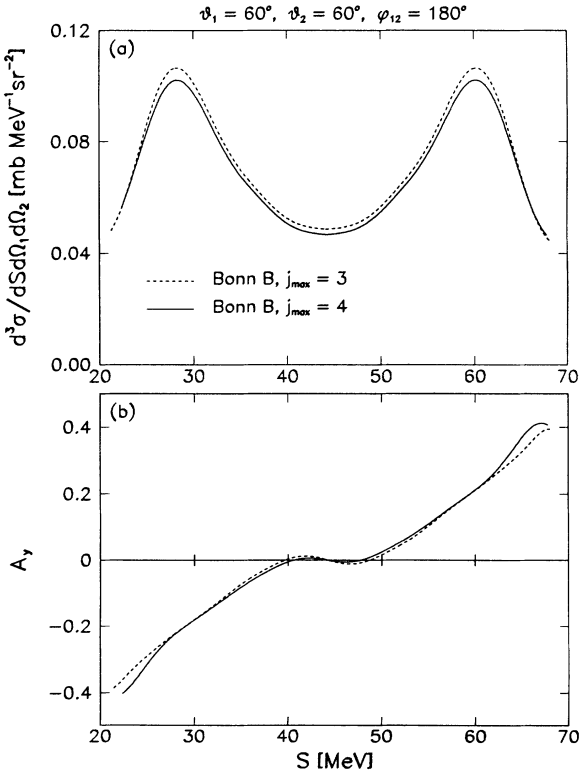

FIG. 12. Convergency test: Predictions of the Bonn B potential for the symmetric configuration (59.5°, 59.5°, 180.0°). The partial waves included for the $2N$ subsystem are $j_{\max} = 3$ (dashed) and $j_{\max} = 4$ (solid). The total angular momentum of the $3N$ system extends to $J_{\max} = \frac{25}{2}$.

V. SUMMARY

The deuteron breakup process induced by polarized protons has been investigated at an incoming proton laboratory energy of 65 MeV in four kinematically complete configurations. Both the differential cross sections and the analyzing powers have been measured. It has been shown that the instrumental resolution effects are negligible in the phase space of interest and a direct comparison with the theoretical observables calculated for

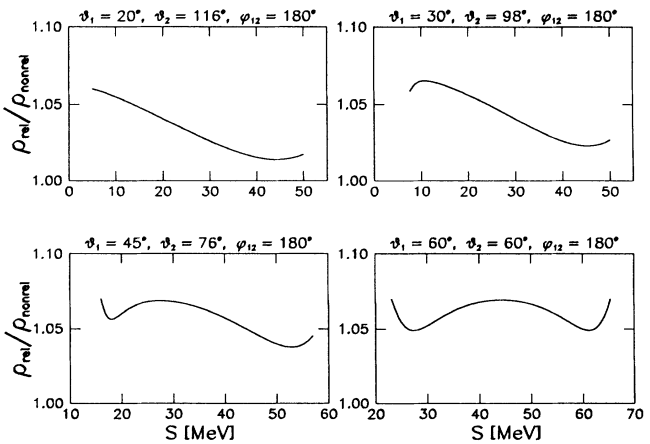

FIG. 13. Ratios of the relativistic and nonrelativistic phase-space factors for four collinearity configurations.

point geometry can be used. The experimental data were then compared to the theoretical predictions based on four realistic potentials: AV14, Bonn B, Nijmegen, and Paris. In the rigorous Faddeev calculations the charge dependence of the $2N$ force in the state $^1S_0$ was taken into account by admitting an admixture of total isospin $T = \frac{3}{2}$. It is gratifying to notice a satisfactory agreement between measured and calculated observables. The theory gives, generally, the correct magnitude and describes the essential structures not only for the cross sections but also for the analyzing powers. If one tries, however, to make a quantitative comparison at an accuracy level compatible with the experimental uncertainties the situation becomes much more subtle. One observes some regions along the three-body kinematics where the discrepancies between theory and experiment lie both outside the experimental uncertainties and the variations of the calculated observables due to different $2N$ potentials.

In this study, special attention was paid to the vicinity of the exact collinearity points. We do not find any intriguing structures neither in the cross sections nor in the analyzing powers. Moreover, the smooth behavior of the observables around these points is well reproduced by the calculation based on pure $2N$ interactions. From the experience at low energy [21,30] it was expected that in the collinearity configurations, which were selected for our experiments, the variations due to different potentials should be especially small. This turned out not to be the case.

The reason for the existing discrepancies between the experimental data and the present theoretical description is unclear. It is, however, remarkable that there is a spread in the theoretical predictions by four different $2N$ potentials used which is comparable in magnitude to the discrepancies between theory and experiment. In view of the equivalence of off-shell $2N$ force and $3N$ force effects [43] in the $3N$ systems it is not unlikely that specific 3NF models, like 2π exchange, might lead to similar effects in the theoretical predictions. Such a calculation including the Tucson-Melbourne 2π-exchange 3NF is planned. Furthermore, an estimation of the influence of the Coulomb forces and of relativistic effects appears highly desirable.

ACKNOWLEDGMENTS

This work has been supported financially by the Swiss National Foundation, the Polish Committee of Scientific Research, Grant PB2598/2/91, and the Deutsche Forschungsgemeinschaft. The numerical work has been performed on the NEC SX-3/22 system at CSCS in Manno, Switzerland.

[1] W. Glöckle, H. Witala, and Th. Cornelius, Nucl. Phys. **A508**, 115c (1990); in *Proceedings of the 25th Zakopane School on Physics*, Selected Topics in Nuclear Structure, edited by J. Styczeń and Z. Stachura (World Scientific, Singapore, 1990), Vol. 2, p. 300.

[2] H. Witala, Th. Cornelius, and W. Glöckle, Few-Body Syst. **3**, 123 (1988).

[3] K. Sagara, H. Oguri, S. Shimizu, H. Nakamura, and T. Nakashima, *Proceedings of the XIII International Conference of Few-Body Problems in Physics*, Adelaide, 1992 (Institute of Atomic Studies, Adelaide, 1992), Report FIAS-R-216, ISSN 0725 783x, p. 284.

[4] G. Rauprich, H. J. Hähn, M. Karus, P. Niessen, H. Oswald, L. Sydow, H. Paetz gen. Schieck, and Y. Koike, Few-Body Syst. **5**, 67 (1988).

[5] W. Grüebler, Nucl. Phys. **A463**, 193c (1987), and references therein.

[6] H. Shimizu, K. Imai, N. Tamura, K. Nishimura, K. Hatanaka, T. Saito, Y. Koike, and Y. Taniguchi, Nucl. Phys. **A382**, 242 (1982).

[7] S. Shimizu, K. Sagara, K. Maeda, H. Nakamura, T. Miwu, N. Nishimori, S. Ueno, and T. Nakashima, *Proceedings of the XIII International Conference of Few-Body Problems in Physics* [3], p. 308.

[8] M. Clajus, P. M. Egun, W. Grüebler, P. Hautle, I. Slaus, B. Vuaridel, F. Sperisen, W. Kretschmer, A. Rauscher, R. Waidmann, A. Glombik, J. Albert, M. Bruno, F. Canatta, M. D'Agostino, and P. A. Schmelzbach, *Proceedings of the XIII International Conference of Few-Body Problems in Physics* [3], p. 116.

[9] L. Sydow, P. Niessen, G. Rauprich, R. Reckenfelderbäumer, S. Vohl, and H. Paetz gen. Schiek, *Proceedings of the XIII International Conference of Few-Body Problems in Physics* [3], p. 120.

[10] C. R. Howel, W. Tornow, K. Murphy, H. G. Pfützner, M. L. Roberts, Anli Li, P. D. Felscher, R. L. Walter, I. Slaus, P. A. Treado, and Y. Koike, Few-Body Syst. **2**, 19 (1987); W. Tornow, C. R. Howel, M. Alohali, Z. P. Chen, P. D. Felscher, J. M. Hanly, R. L. Walter, G. Weisel, G. Mertens, I. Slaus, H. Witala, and W. Glöckle, Phys. Lett. B **257**, 273 (1991).

[11] J. Cub, E. Finckh, M. Friess, G. Fuchs, K. Gebhardt, K. Geissdörfer, R. Lin, and J. Strate, Few-Body Syst. **6**, 151 (1989).

[12] J. E. McAninch, W. Haeberli, H. Witala, W. Glöckle, and J. Golak, Phys. Lett. B **307**, 13 (1993).

[13] H. Rühl, B. Dechant, J. Krug, W. Lübcke, G. Spangardt, M. Steinke, M. Stephan, D. Kamke, J. Balewski, K. Bodek, L. Jarczyk, A. Strzalkowski, W. Hajdas, St. Kistryn, R. Müller, J. Lang, R. Henneck, H. Witala, Th. Cornelius, and W. Glöckle, Nucl. Phys. **A524**, 377 (1991).

[14] W. von Witsch, private communication.

[15] G. Janson, L. Glantz, A. Johansson, and I. Kaersner, *Proceedings of the 10th International Conference of Few-Body Problems in Physics*, Karlsruhe, 1983 (North-Holland, Amsterdam, 1984); G. Janson, Ph.D. thesis, University of Uppsala, 1985.

[16] A. C. Berick, R. A. Riddle, and C. M. York, Phys. Rev. **174**, 1105 (1968).
[17] J. Balewski, K. Bodek, L. Jarczyk, B. Kamys, St. Kistryn, A. Strzalkowski, W. Hajdas, J. Lang, R. Müller, B. Dechant, J. Krug, W. Lübcke, H. Rühl, R. Henneck, H. Witala, W. Glöckle, and J. Golak, submitted to Nucl. Phys. A.
[18] H. Witala, D. Hüber, and W. Glöckle, Phys. Rev. C **49**, R14 (1994).
[19] W. Lübcke, Ph.D. thesis, Ruhr-Universität Bochum, 1992.
[20] K. Gebhardt, W. Jäjer, M. Vitz, E. Finckh, T. N. Frank, Th. Januschke, W. Sandhas, and H. Haberzettl, Nucl. Phys. **A561**, 232 (1993).
[21] G. Rauprich, S. Lemaitre, P. Niesen, K. R. Nyga, R. Reckenfelderbäumer, L. Sydow, H. Paetz gen. Schieck, H. Witala, and W. Glöckle, Nucl. Phys. **A535**, 313 (1991).
[22] J. Strate, K. Geissdörfer, R. Lin, W. Bielmeier, J. Cub, A. Ebneth, E. Finckh, H. Friess, G. Fuchs, K. Gebhardt, and S. Schindler, Nucl. Phys. **A501**, 51 (1989).
[23] M. Karus, M. Buballa, J. Helten, B. Laumann, R. Melzer, P. Niessen, H. Oswald, G. Rauprich, J. Schulte-Uebbing, and H. Paetz gen. Schieck, Phys. Rev. C **31**, 1112 (1985).
[24] B. Dechant, Ph. D. thesis, Ruhr-Universität Bochum, 1992.
[25] F. Foroughi, H. Vuilleme, P. Chatelain, C. Nussbaum, and B. Favier, J. Phys. G **11**, 59 (1985).
[26] St. Kistryn, W. Hajdas, J. Lang, R. Müller, J. Balewski, K. Bodek, L. Jarczyk, B. Kamys, A. Strzalkowski, B. Dechant, J. Krug, W. Lübcke, H. Rühl, G. Spangardt, M. Steinke, M. Stephan, D. Kamke, H. Witala, Th. Cornelius, W. Glöckle, and J. Golak, Nucl. Phys. **A548**, 49 (1992).
[27] M. Stephan, K. Bodek, J. Krug, W. Lübcke, S. Obermanns, H. Rühl, M. Steinke, D. Kamke, H. Witala, Th. Cornelius, and W. Glöckle, Phys. Rev. C **39**, 2133 (1989).
[28] D. Hüber, H. Witala, and W. Glöckle, Few Body Syst. **14**, 171 (1993).
[29] W. Meier and W. Glöckle, Phys. Lett. **138B**, 329 (1984).
[30] H. Witala, W. Glöckle, and Th. Cornelius, Phys. Rev. C **39**, 384 (1989).
[31] P. D. Eversheim, F. Hinterberger, U. Lahr, B. von Przewoski, J. Campbell, J. Götz, M. Hammans, R. Henneck, G. Masson, and I. Sick, Phys. Lett. B **234**, 253 (1990).
[32] J. E. Durisch, W. Neumann, and J. Rossel, Nucl. Instrum. Methods **80**, 1 (1970).
[33] M. Ieiri, H. Sakaguchi, M. Nakamura, H. Sakamoto, H. Ogawa, M. Yosoi, T. Ichihara, N. Isshiki, Y. Takeuchi, H. Toawa, T. Tsutsumi, S. Hirata, T. Nakano, S. Kobayashi, T. Noro, and H. Ikegami, Nucl. Instrum. Methods A **257**, 253 (1987).
[34] J. Smyrski, Ph. D. thesis, Jagellonian University, Cracow, 1988.
[35] A. Converse, W. Haeberli, W. Hajdas, St. Kistryn, J. Lang, J. Liechti, H. Lüscher, R. Müller, J. Smyrski, and J. Sromicki, Phys. Rev. C **45**, 2320 (1992).
[36] G. G. Ohlsen, Nucl. Instrum. Methods **37**, 240 (1965).
[37] W. Glöckle, *The Quantum-Mechanical Few-Body Problem* (Springer-Verlag, Berlin, 1983); *Lecture Notes in Physics*, Vol. 273 (Springer, Berlin, 1987), p. 3.
[38] R. B. Wiringa, R. A. Smith, and T. L. Ainsworth, Phys. Rev. C **29**, 1207 (1984).
[39] R. Machleidt, Adv. Nucl. Phys. **19**, 189 (1989).
[40] M. M. Nagels, T. A. Rijken, and J. J. de Swart, Phys. Rev. D **17**, 768 (1978).
[41] M. Lacombe, B. Loiseau, J. M. Richard, R. Vinh Mau, J. Cote, P. Pires, and R. de Tourreill, Phys. Rev. C **21**, 861 (1980).
[42] H. Witala, W. Glöckle, and H. Kamada, Phys. Rev. C **43**, 1619 (1991).
[43] W. Polyzou and W. Glöckle, Few-Body Syst. **9**, 97 (1990).

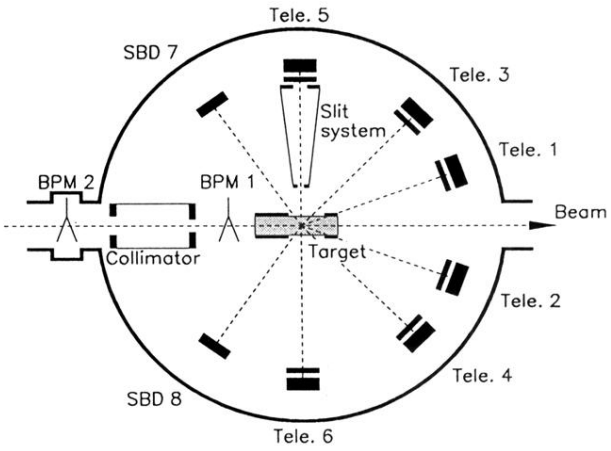

FIG. 1. Experimental setup in the scattering chamber—schematic diagram. The collimating system for only one detector is shown. BMP1 and BMP2 are the beam profile monitors.

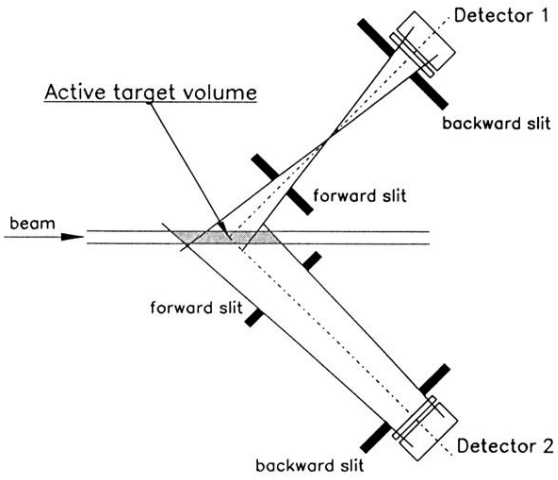

FIG. 2. Effective target volume. The collimator of detector 1 defines the target volume which is entirely seen by detector 2.